COMPARISON OF MICROSTRUCTURE AND NON-METALLIC INCLUSIONS IN TOP-FILLED AND BOTTOM-FILLED GRAY IRON CASTINGS

Evan Carter, Jingjing Qing and Mingzhi Xu
Georgia Southern University, Statesboro, GA, USA

https://doi.org/10.1007/s40962-024-01356-y

Abstract

A bottom-filled rigging system was designed to produce gray iron castings, which was compared with a top-filled design in the present study. Filling and solidification of gray iron produced with the bottom-filled mold were compared with that for the top-filled mold. At similar cooling rate and solidification condition, the count of Type A graphite flakes was greater in the bottom-filled casting, while its graphite flakes were also finer in size. In addition, the statistical analysis of non-metallic inclusions using a scanning electron microscope equipped with auto feature analysis software also showed differences in inclusion composition, size, and population density between two castings. The results indicated that the filling turbulence promoted interactions between metal with air, which in turn influenced the formation of non-metallic inclusions. As a result, this impacted the nucleation of flake graphite in the gray iron.

Keywords: *gray iron, bottom-filled gating, top-filled gating, air entrapment, graphite inclusions, cleanliness*

Introduction

Gray iron is an iron-carbon-silicon alloy, and it is the most used cast iron in industrial applications. It has superior machinability, excellent thermal conductivity, and it dampens vibrations. A large fraction of carbon in the gray iron precipitates out as the graphite phase, which appear as black flakes in the iron matrix under an optical microscope. A micrograph of gray iron is shown in Figure 1. Type A flakes are desired in most grades of gray iron and they appear in long and moderately curly flakes. Three-dimensionally, graphite flakes form interconnected networks, unlike in the ductile iron where graphite nodules are separated by the iron matrix. These interconnected networks of graphite provide easy paths for conducting heat.[1–3] Formation of the straighter and longer flakes, Type C flake graphite (also called kish graphite), can further improve the thermal conductivity in the hypereutectic gray iron. The flake graphite networks in the gray iron provide it with high thermal conductivity and vibration dampen properties.

The mechanical and physical properties of cast irons depend both on the graphite phase and the surrounding matrix. It is well documented that the morphology (shape, size, and distribution) of graphite, the composition, type of phase, and the fineness of the matrix microstructure will impact the properties of gray iron.[2,4–10] In addition to the graphite and matrix, non-metallic inclusions (e.g., oxides, nitrides, and sulfides) are commonly observed in the microstructure of gray irons. Shape, size, count, and distribution of the non-metallic inclusions also directly impact the mechanical properties of gray iron. For example, hard to deform inclusions that are angular or cuboidal shaped will cause stress concentrations.[11–14] Stress concentrations will accelerate cracking and failure of the component, i.e., reduce its strength, toughness, and fatigue limit.

Non-metallic inclusions in metallic alloys may be classified as endogenous or exogenous types. Exogenous inclusions originate from external sources and are entrapped in the cast alloy (e.g., refractory, slag, and sand). Endogenous inclusions are those precipitated in the metals due to chemical interactions during solidification and cooling. In foundry practice, using a ceramic filter in the gating system can lower the number of exogenous inclusions entering the casting. The endogenous inclusions may appear as liquid

This paper is based upon one in the 2024 AFS Transactions Vol. 132.
Received: 20 March 2024 / Accepted: 10 April 2024 /
Published online: 10 May 2024

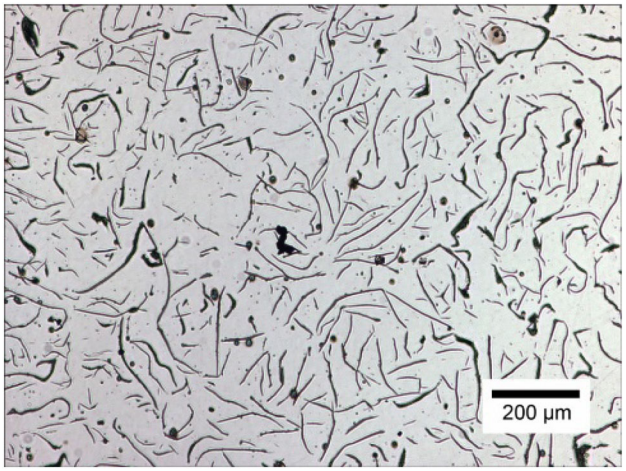

Figure 1. Micrograph of an unetched gray iron sample showing the flake graphite in the matrix (50×).

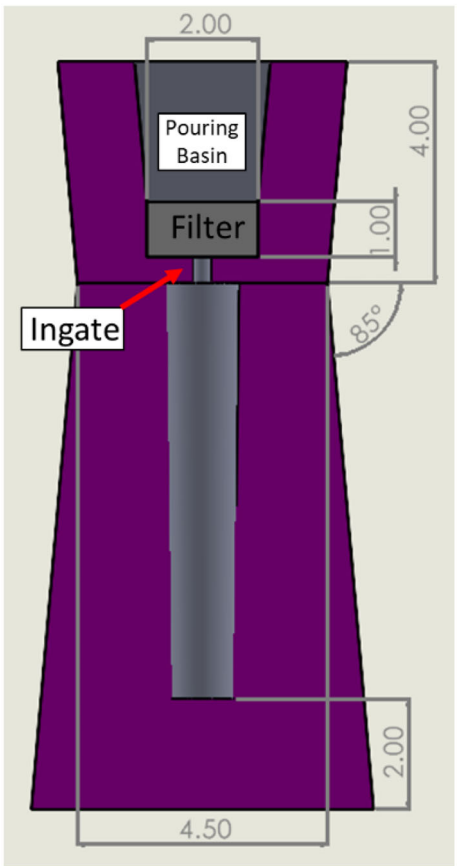

Figure 2. A 2D drawing of the top-filled casting design, dimensions are in inches.

phase or solid phase, and the filter can capture both liquid and solid inclusions. However, as the micropore of a filter is saturated, large-sized liquid inclusion particles may be released back in the metal.[14] In gray iron, non-metallic inclusions also perform critical roles in nucleating graphite. Studies have shown that complex manganese oxysulfide

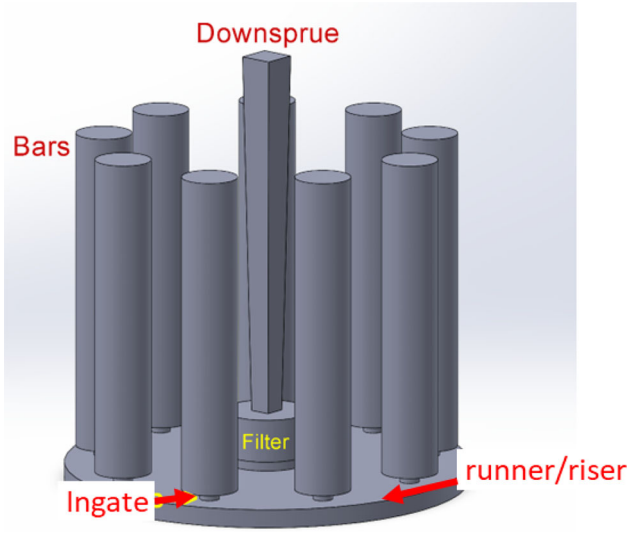

Figure 3. Solid model showing the arrangement of 9 test bars in the bottom-filled design.

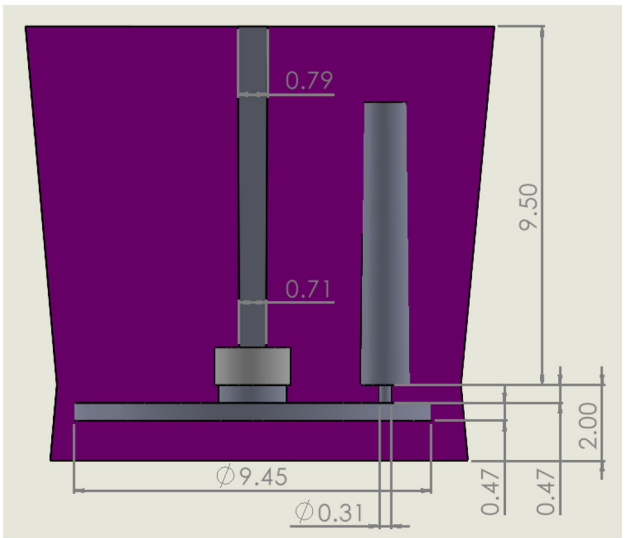

Figure 4. A 2D drawing of the bottom-filled casting design, dimensions are in inches.

inclusions nucleated by oxides are the main nucleation site providers during graphite formation.[6,15,16]

Tensile properties are important considerations in the component designs using gray irons. Design engineers usually select a grade of gray iron based on its tensile strength. Grades of commercial gray irons are normally classified based on their tensile strengths. The ASTM A-48 standard classifies gray irons in terms of tensile strength, and also includes a recommendation for the mold design to produce standard tensile testing bars for gray irons.[17] The gating design suggested in the ASTM A48 standards adopts a top-filled gating system. The metal stream free falling through a top-filled gating system above the casting cavity is highly turbulent, and a bottom-filled gating system is more desired when the turbulence during filling needs to be

minimized for preventing casting defects. Air may be entrapped due to the turbulent flow. The filling velocity through a bottom-filled gating system can be slowed down. In addition, a filter is typically added in the gating system above the tensile bar castings to filtrate inclusions in the molten metal.[14,18] The liquid metal stream traveling through the filter will diverge into numerous finer streams, and the flow of the metal stream will be slowed down. The resulting rainfall of metal streams will significantly increase the surface area of molten metal in contact with air. The interactions between metal and air will increase the population of non-metallic inclusions (e.g., nitrides and oxides) in the casting, which may impair its mechanical performance. Additional oxide inclusion formation and growth may impact the formation of Mn–O–S inclusions, which in turn affects graphite nucleation during solidification. However, this phenomenon has not received adequate attention within the research community.

The objective of this research is to reveal the advantages of the bottom-filled rigging system compared to the top-filled rigging design, to produce gray iron castings of better quality. In this research, a bottom-filled rigging system was designed to produce gray iron tensile bar castings, which were compared with a top-filled design. The bottom-filled gating system offers advantages including non-turbulent flows during filling and reduced air entrapment. This bottom-filled gating design can be customized to produce multiple bars in a single mold. A bottom riser was incorporated in the design to promote optimal directional solidification. Computational simulations were performed to reveal the differences in filling and solidification of gray iron in the two mold designs. Graphite flakes and non-metallic inclusions in the gray iron castings were characterized and compared for the top-filled and bottom-filled gating designs. Thermodynamic simulations were adopted to better understand the interactions between the gray iron melt and air. It is postulated that the gating design can change the thermodynamics of interactions between gray iron and air, and leading to variations of microstructure (graphite size, count, and inclusions) in gray irons.

Table 1. Chemistry of the Inoculant Used in this Research

	Si	Ca	Al	Ti	Mn
wt.%	74.26	0.98	1.05	0.133	0.12
	P	C	Cr	Fe	
wt.%	0.007	0.016	0.03	Bal.	

Design of Experiments

Mold Design

In this study, two castings were designed and poured to produce ASTM A48 size B tensile test bars. The first casting closely adhered to the specifications suggested by the ASTM A48 standard. A 10 ppi SiC ceramic foam filter between the pouring basin and ingate was used in this top-filled mold design. Notable specifications set by the standard are the mold wall thickness and ingate dimensions. The minimum wall thickness is equal to the maximum diameter of the test bar, 1.32 in. (33.5 mm), and the inlet is a cylinder with 1/8 in. (3.2 mm) diameter and 3/16 in. (4.8 mm) height. Figure 2 is a schematic showing the geometry of the casting and mold layout. The purple areas indicate the mold volume, the gray area indicates the casting volume, and the filter volume is shown in the lighter gray area.

The second design incorporated a bottom-filled gating system, and maintained the notable standard specifications mentioned before. The ingate dimensions and the mold thickness of the bottom-filled design were kept the same as the top-filled design. The bottom-filled gating system was designed to minimize the turbulence during filling. Additionally, the bottom-filled casting was designed to produce 9 test bars (Figure 3). Exact dimensions of the bottom-filled design are listed in Figure 4. For the bottom-filled design, pouring basin (not shown), down sprue, vents, filter, and a cylindrical disc runner/riser (9.4 in. or 240 mm diameter) were added. A 10 pores-per-inch (ppi) SiC ceramic foam filter was used. A core was included in the mold above the bottom disc runner/riser to create the ingate features.

Filling and solidification of gray iron in the two casting designs were simulated using computational software. Based on the computational simulations, dimensions for

Table 2. Chemical Composition of the Gray Iron Used for This Study

	C	Si	S	P	Ni	Mo	Mn
wt.%	3.23	2.00	0.082	0.016	1.03	0.47	0.58

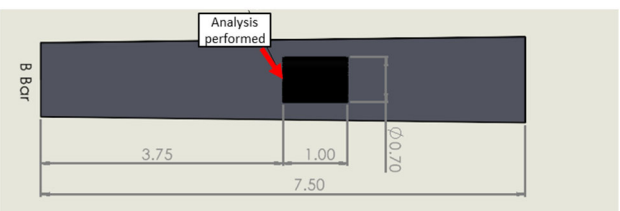

Figure 5. Schematic showing the metallographic sample locations in the cast test bar, dimensions are in inches.

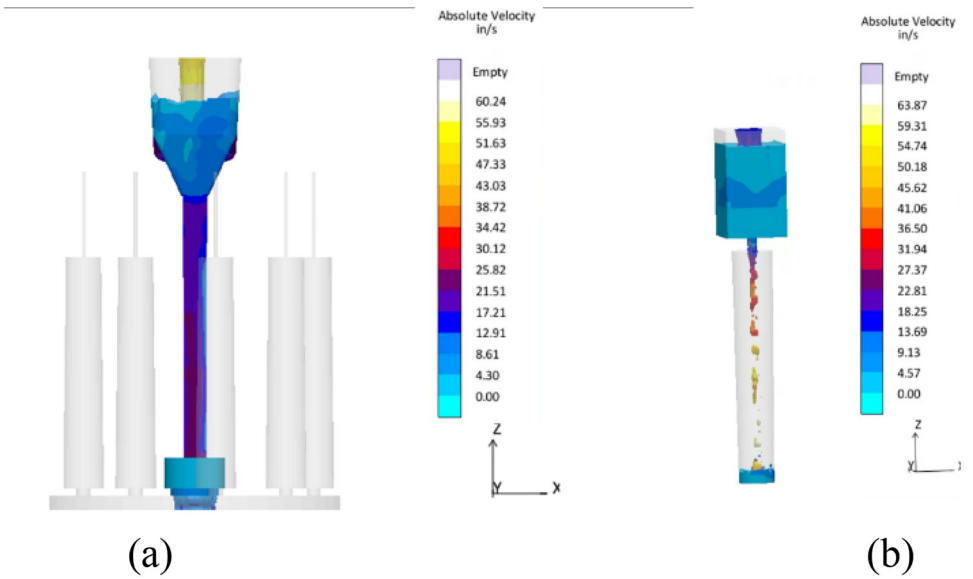

Figure 6. Velocity of the molten metal at 1.4 s (prior to priming of filter) of pouring in (a) bottom-filled and (b) top-filled molds.

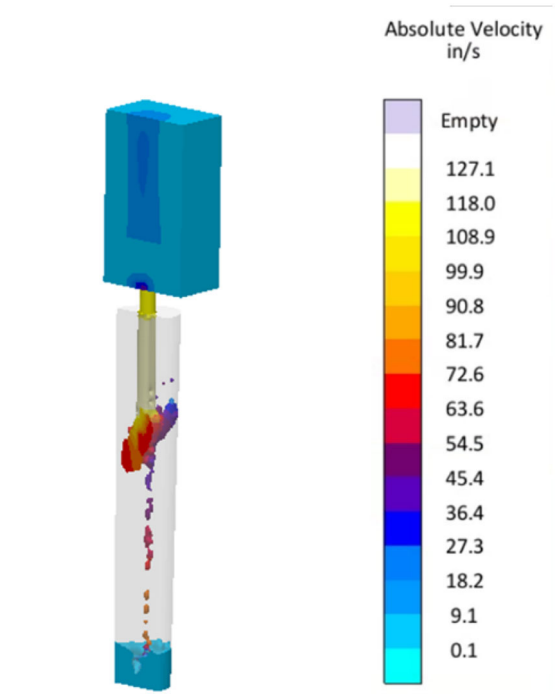

Figure 7. Velocity of the molten metal at 1.6 s (filter has been primed) of pouring showing the change in metal stream flow in the top-filled mold.

the gating system were optimized for the bottom-filled mold. The simulation results also aided the analysis of filling results, solidification results, and casting defect results.

Patterns for the molds were produced and assembled using wood and 3D printed polymer. No-bake molds were made

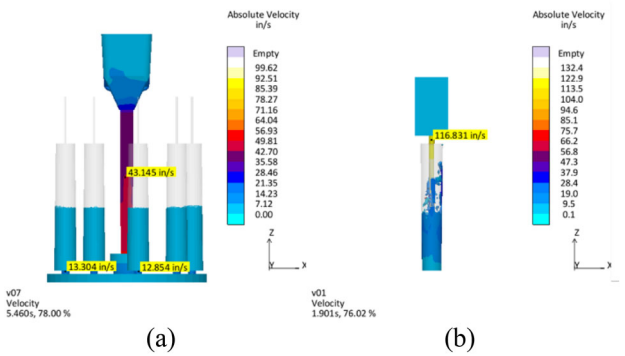

Figure 8. Molten metal velocity at ingate when test bars were approximately 50% full the in (a) bottom-filled and (b) top-filled molds.

with silica sand and ester-cured phenolic resin. The no-bake sand mixture has 1.5 wt.% resin and 0.5 wt.% co-reactant.

Metal Preparation and Pouring

A hypoeutectic gray iron (3.3C–2.0Si–0.5Mn–0.08S) was selected in this study. Ni and Mo were added for another study requiring post heat treatment. A 100-lb. medium-frequency coreless induction furnace was used to melt the charge materials. The charge materials used included pig iron, steel scrap, graphite, ferrosilicon, ferromanganese, nickel, ferromolybdenum, and iron sulfide. Air melting without covering gas ensures that the oxygen and nitrogen concentrations are closer to the equilibrium levels, and sulfur concentration was also raised to the targeted value. After all charge materials melted and a temperature of

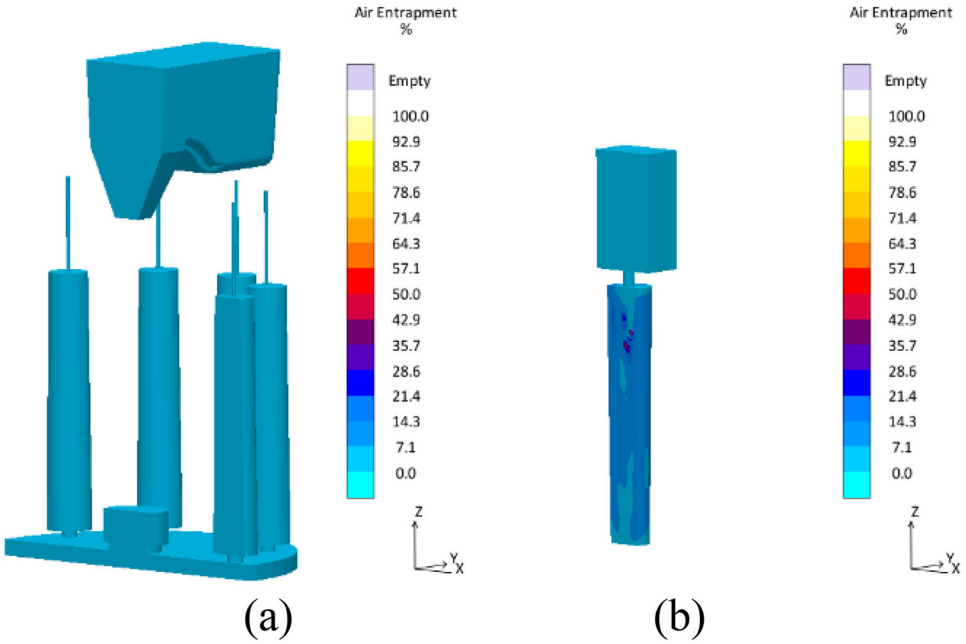

Figure 9. Air entrapment in the test bars at the end of filling in (a) bottom-filled and (b) top-filled molds.

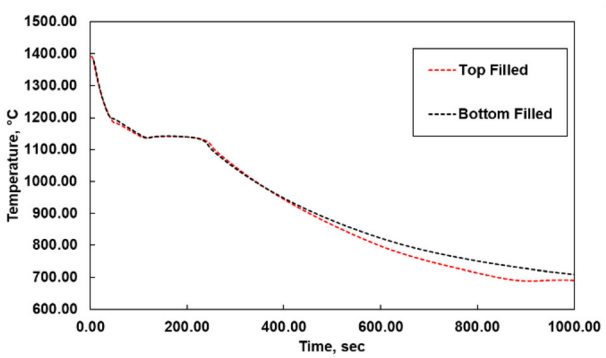

Figure 10. Cooling curves from the center of the test bar in top-filled and bottom-filled molds.

1470 °C (2678 °F) is achieved in the molten metal, a chemistry sample was taken from furnace, and the chemistry was trimmed to meet the target chemistry. The liquid metal was then brought to 1530 °C (2786 °F) and held for approximately 10 min to ensure dissolutions of the additions introduced during chemistry trim. This holding duration also helps to achieve equilibrium oxygen and nitrogen levels in the melt. The iron was then tapped into a preheated 100-lbs. ladle with the in-ladle inoculant at 1505 °C (2741 °F). The inoculant addition rate is 0.15 wt.%, and the composition of the inoculant is shown in Table 1. The same heat was poured to fill both the top-filled and bottom-filled molds. After pouring, the castings were left to cool in molds overnight. The composition of the final castings is shown in Table 2. Weight percentages of C and S were determined with a combustion analyzer. The remainder of the composition was measured with an optical emission spectrometer.

Metallographic Analysis

Two metallographic samples were sectioned from the center of the test bars in the castings, after shaking out the castings from the mold. Metallographic examinations were performed on the sectioned face in the middle of test bars. Figure 5 shows the locations of the samples for metallography. The two metallographic samples were ground and polished following standard metallographic procedure, and the finish step was 0.1 micron diamond paste polishing.

Metallographic samples were examined using an optical microscope. In addition, non-metallic inclusions in the metallographic samples were statistically analyzed using a scanning electron microscope equipped with an EDX (energy-dispersive X-ray) detector and auto feature analysis software (AFA). The scanning electron microscope (SEM) was operated under a 15.0 kV acceleration voltage. The SEM-EDX-AFA algorithm is widely used by the steel industry for inclusion analysis. The SEM-AFA algorithm selects features of interest based on designated brightness levels. The SEM automatically scans through the defined area and searches for the features satisfying the brightness threshold, and backscattered electron (BSE) image of the feature of interest will be captured and image analysis will be performed automatically. In the meantime, the chemical composition of the feature will be also collected based on the EDX analysis. This SEM-EDX-AFA function allows statistical analysis of a large population of features of interest and generates information on size, shape, distribution, and chemical composition for the features. An area of 15.8 mm^2 (0.024 $in.^2$) was scanned and analyzed at the center of each specimen for non-metallic inclusion

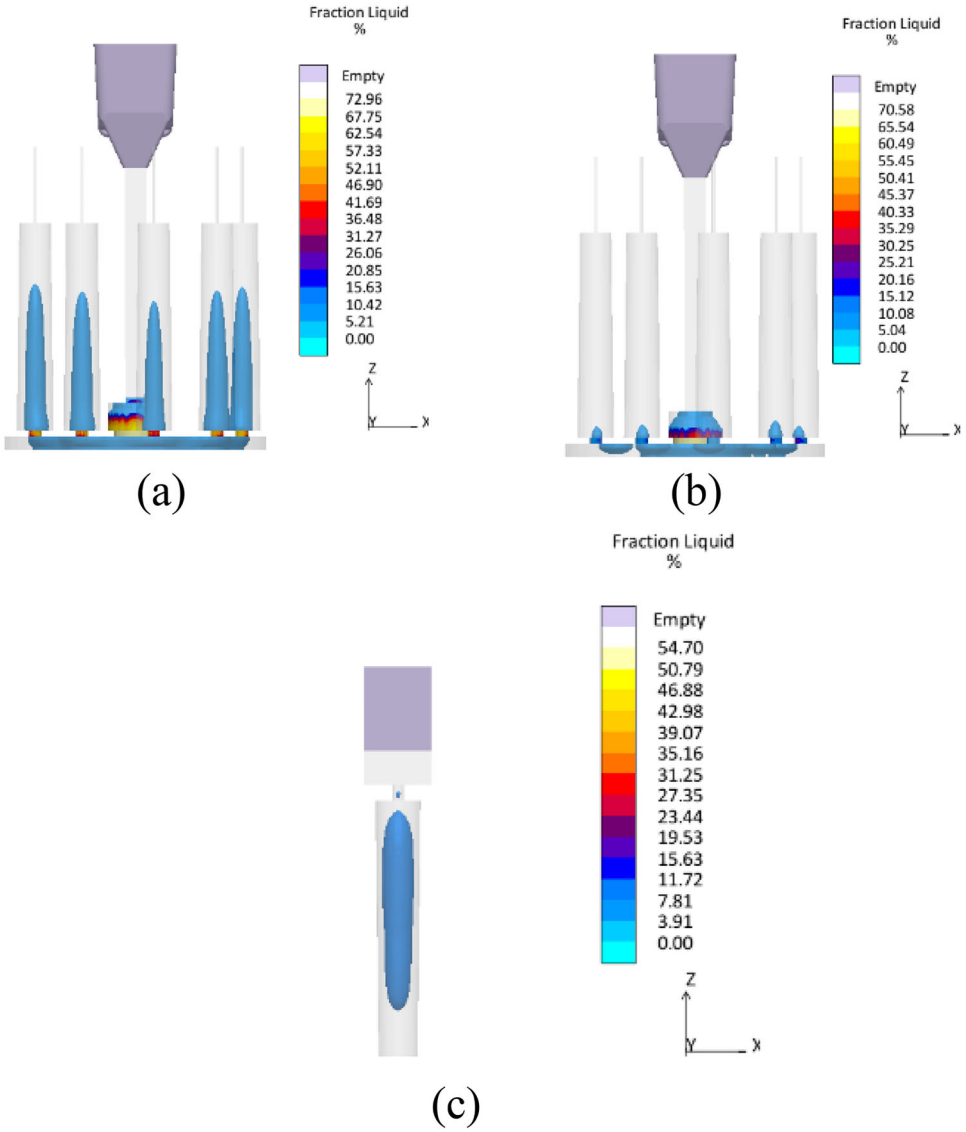

Figure 11. Liquid fractions in (a) bottom-filled mold when the bar partially solidified, (b) bottom-filled mold when the bar mostly solidified, and (c) top-filled mold during solidification.

analysis. Over 10,000 features (including flake graphite and non-metallic inclusions) were analyzed for each sample. Rules for classifying the type of non-metallic inclusions were tailored for the gray iron used in the present study, and the major elements in the different inclusions were plotted in the ternary diagrams to show their compositions.

Results and Discussion

Filling and Solidification Simulation

The computational software used for simulations of filling and solidification showed drastically different results, regarding the flow of the metal. Figure 6a, b compare the simulated molten metal velocity at 1.4 s of the pour prior to priming of the ceramic filter. For the bottom-filled casting, the metal did not begin feeding the test bars during the free fall of metal. In contrast, the top-filled casting experienced free fall of liquid metal for nearly the entire duration of the filling. Additionally, the top-filled casting had small and discreate streams of liquid metal falling into the cavity before the filter was properly primed. A sudden increase in velocity through the ingate in the top-filled mold was also observed after 1.6 s when the filter was primed, and the pressure was increasing as the pouring basin was filled. Not only did this increase the metal velocity beyond the recommended limits for gray iron castings, but it also caused more turbulence as the rainfall-like stream transformed into a geyser-like stream of metal. Figure 7 shows the resulting phenomenon of a large front of high-speed liquid metal about to impact and mix with the initial metal pool. Figure 8a, b compares the velocities of metal at ingates when the bars are roughly 50% full. The top-filled casting

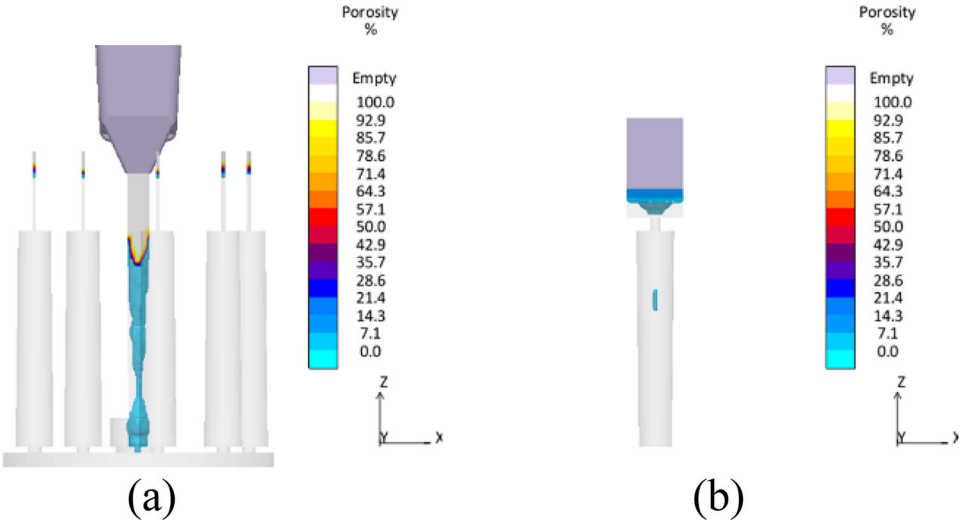

Figure 12. The final shrinkage porosity distribution in (a) bottom-filled and (b) top-filled molds.

showed a metal velocity at the ingate to be roughly nine times higher than that for the bottom-filled casting. Additionally, the metal velocity at top-filled ingate well exceeded the typical maximum allowed velocity for gray iron gating design, 1.0 m/s (40 in./s). The combination of speed and variation in flow caused swirling of the metal. Additionally, the top-filled gating design broke down the metal stream to finer streams and increased exposes surface area in contact with air which in turn accelerated reaction of metal with air. The subsequent increase in metal filling velocity caused turbulence and increased air entrapment during mixing, and splash of metal can be seen in Figure 8b. The bottom-filled casting had a smooth and even filling across all bars, and the velocities of the liquid metal after the filter always stayed below the recommended maximum velocity. The air entrapment results for the top-filled casting were drastically higher, as expected, than the bottom-filled casting. For most of the filling time, the air entrapment in the top-filled casting had readings above 80 percent. As the simulation proceeded toward the end of filling, air entrapment further increased. At the end of filling (Figure 9), the top-filled casting had a maximum air entrapment of 98%, while the bottom-filled casting had a maximum air entrapment of 2%.

Solidification simulation was also performed using computational software. Cooling rates and solidification times for test bars in both mold designs were nearly identical, based on the simulated cooling curves at center of the test bar as shown in Figure 10. Similar cooling rates allow comparison of the microstructure (e.g., flake graphite size and count) in the test bars produced with the two gating designs. Despite the temperature curves being similar, the solidification patterns of the top-filled and bottom-filled castings were different. Liquid fractions during solidification in both molds are compared in Figure 11a–c. The bottom-filled casting experienced improved directional solidification when compared to the top-filled casting. This was because the bottom disc runner/riser had a high enough modulus to shift the last solidified region away from the test bars, as demonstrated in Figure 11a, b. Directional solidification in the bottom-filled casting pushed the last-to-freeze zone away from the test bars. As shown in Figure 11c, the last solidified region in the top-filled test bar was in the bar, but it was isolated from the pouring basin/riser during the solidification so that the feeding of metal to the last to solidified zone became impossible. Shrinkage porosity prediction of the two castings in Figure 12a, b showed that the bottom-filled casting had less porosity. It is also worth noting that the location with maximum air entrapment in the top-filled casting (Figure 9) coincides with the shrinkage porosity location, and it is likely that the shrinkage porosity and gas porosity (due to air entrapment) will compound to increase the likelihood of problematic casting defects in the center of the test bar. Additionally, the difference in yield between the mold designs is low. The top-filled mold design has a yield of 50% and the bottom-filled design has a yield of 43%.

Graphite Quantification

Figure 13a, b is the micrographs of the unetched samples from the bottom-filled casting and top-filled casting, respectively. Both samples showed clear Type A flake graphite morphology. SEM-EDX-AFA analyses were performed on both samples to statistically characterize the graphite flakes as well as the non-metallic inclusions in the microstructure. Numbers and areas of graphite flakes over an area of 15.8 mm^2 observed in the 2D cross section at the center of each sample are shown in Table 3. The overall graphite area percentage were found to be similar between the bottom-filled and top-filled samples. The bottom-filled test bar, however, had a higher count of graphite flakes than

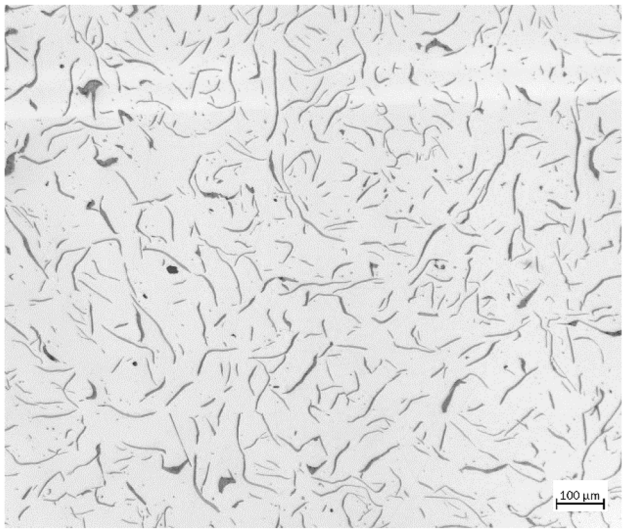

(a)

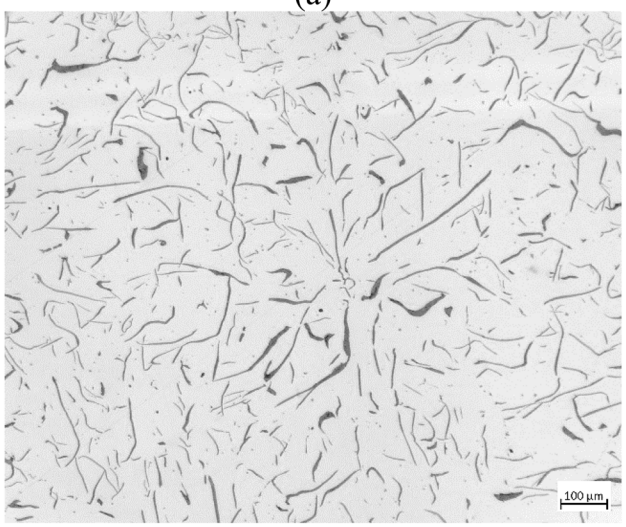

(b)

Figure 13. Unetched microstructure at the center of (a) bottom-filled test bar and (b) top-filled test bar (100×).

Table 3. Graphite Number Density and Area Percent Over an Area of 15.8 mm² (0.024 in.²) in the Compared Test Bars

	Graphite number density, /mm²	Graphite area percent, %
Bottom-filled test bar	545.9	8.78
Top-filled test bar	466.4	8.98

the top-filled test bar. SEM-AFA analysis measures perimeter (p) and area (A) of each individual graphite feature. The average length (l) and thickness (t) of a given graphite flake can be estimated using the following equations:

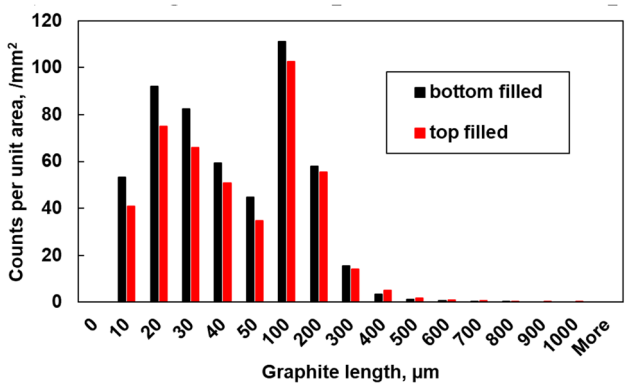

(a)

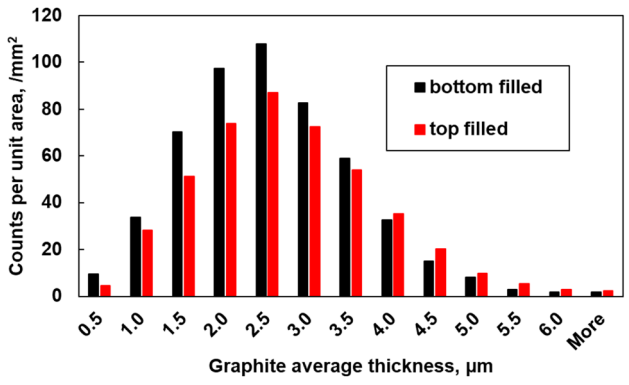

(b)

Figure 14. Distributions of (a) graphite length and (b) average thickness in bottom-filled and top-filled test bars.

Table 4. Number Density and Area Percentage of Inclusions Classified Through SEM-EDX-AFA

Inclusion types	Number density, /mm²		Area percentage, %	
	Bottom-filled	Top-filled	Bottom-filled	Top-filled
Simple MnS	867.9	789.5	0.348	0.342
Complex MnS	92.3	82.7	0.033	0.035
Other oxides	37.3	38.7	0.014	0.019
Other nitrides	91.5	93.3	0.022	0.148

$$l = p \times 0.5$$
$$t = A/l = 2 \times A/p$$

Distributions of graphite length and average thickness are shown in Figure 14a, b, respectively. It can be seen that the bottom-filled test bar had a higher population of graphite flakes, and the graphite flakes are finer compared to the

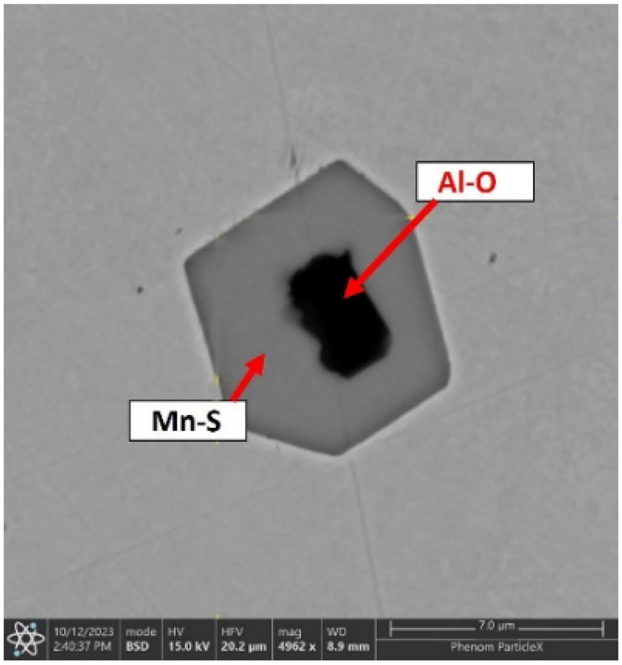

Figure 15. SEM backscattered electron image of a complex MnS inclusion with an Al–O core.

top-filled test bar, even though both samples have similar area percentage of graphite. As mentioned before, the cooling rate and the solidification time for both castings were comparable according to Figure 10. The authors postulate that the different graphite size distribution was not due to cooling rate or solidification differences, but was caused by the difference in inoculation conditions when non-inclusion formations were varied between bottom-filled and top-filled molds.

Non-metallic Inclusion Quantification

Non-metallic inclusions captured and analyzed by SEM-EDX-AFA were classified based on their chemical compositions. Number density and area percentage for the different classified types of inclusions are listed in Table 4. In specific, complex MnS inclusions are the MnS inclusions that had discernable nuclei for MnS within the individual inclusion. Common nucleation sites of MnS found in this analysis consisted of Al_2O_3 and Ti(CN). Thermodynamic calculation using FactSage 8.2 and FS-Steel database showed that Al_2O_3 and Ti(CN) are solid inclusions at the pouring temperature, comparing to MnS which did not form until eutectic solidification at around 1154 °C (2109F). An example of complex MnS inclusions with an Al_2O_3 core is shown in Figure 15.

Compositions of the Mn, Al, and Ti in the sulfide inclusions analyzed in both samples are presented using the ternary diagrams in Figure 16. Based on the literature survey,[6,15,16,19] complex MnS inclusions are more effective

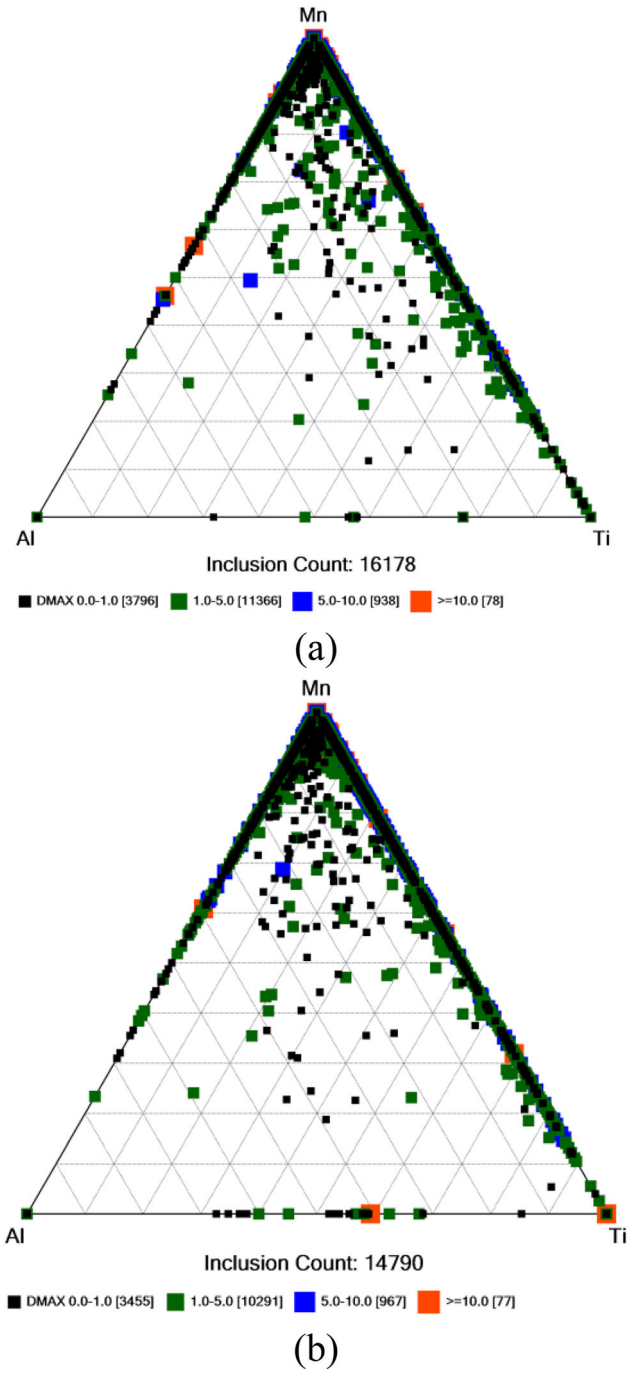

Figure 16. Ternary diagrams showing composition of Mn, Al, and Ti in sulfide inclusions detected in (a) bottom-filled and (b) top-filled test bars.

in nucleating Type-A flake graphite in gray irons. According to Table 4, the area percentage of MnS inclusions (including both simple MnS and complex MnS) was comparable in bottom-filled and top-filled castings. The bottom-filled castings, however, had approximately 12% higher number counts of Mn containing sulfide (both simple and complex) inclusions, and the sizes of these sulfide inclusions are smaller. Recall that the graphite flakes in the bottom-filled casting were also finer according

to Figures 13 and 14. This implies that the higher counts and smaller sizes of MnS inclusions in the bottom-filled casting are more suitable to nucleate a higher population of graphite flakes. In addition, area percentages of oxide and nitride inclusions in the top-filled casting were higher than that of bottom-filled casting, which indicated more severe interactions between the gray iron melt and the air. Such severe reoxidation led to undesired size or chemical compositions of oxides, which "poisoned" the nucleation of Mn containing sulfides suitable for flake graphite nucleation. Based on the inclusion analysis, highly turbulent flow, and greater exposure to air of the metal in the top-filled mold had in the gray iron, and in turn affected the nucleation of flake graphite.

Summary

A bottom-filled rigging was designed to produce gray iron tensile bars. Computational fluid dynamic simulation was used to compare filling and solidification of metal in the bottom-filled design with another top-filled design following ASTM A48 standard. The bottom-filled design was able to achieve a smoother filling, and the velocity at the ingate was below critical filling velocity for gray iron. Simulation also indicated reduced shrinkage porosity in the bottom-filled mold design.

Gray iron test bars were produced in both top- and bottom-filled molds. Graphite flakes and non-metallic inclusions in the test bars were statistically analyzed using SEM-EDX-AFA. Comparisons showed bottom-filled test bars had a higher population and finer graphite flakes, indicating more effective nucleation of graphite flakes. This was attributed to the larger population of Mn containing sulfide or complex sulfide inclusions with appropriate fine sizes that can serve as effective heterogeneous nuclei of Type A flake graphite in the bottom-filled casting. Moreover, higher area percentages of oxides and nitrides were observed in the top-filled casting, due to larger surface areas and longer time exposed to the air, and thus more severe reactions between metal and air. The more severe reactions between air and metal either led to undesired size or chemical compositions of oxides, which "poisoned" the nucleation of Mn containing sulfides suitable for flake graphite nucleation. Highly turbulent flow and greater exposure to air for the metal in the top-filled mold changed the thermodynamics of non-metallic inclusions in the gray iron, and in turn affected the nucleation of flake graphite.

Future Work

Mechanical testing will also be performed in the future. In the bottom-filled design, directional solidification is achieved. Additional evaluations on impacts on microstructure and mechanical properties and comparison to the those adopting the current ASTM bar mold design will be conducted in the future.

Acknowledgements

Part of this work was funded by the American Foundry Society (AFS). The authors appreciate the discussions with the AFS Cast Iron Technical Committee members. The assistance on experiments from fellow graduate and undergraduate students at Georgia Southern University are also acknowledged. This paper is based upon a presentation made at the 2024 AFS Metalcasting Congress and published in the 2024 AFS Transactions Vol. 132.[20] The authors also want to acknowledge the National Science Foundation for supporting the research team to develop the inclusion classification and graphite characterization methodology.

REFERENCES

1. G. Rivera, P.R. Calvillo, R. Boeri, Y. Houbaert, J. Sikora, Examination of the solidification macrostructure of spheroidal and flake graphite cast irons using DAAS and ESBD. Mater Charact **59**, 1342–1348 (2008)
2. B. Wang et al., Microstructure refinement and strengthening-toughening mechanisms of gray cast irons reinforced by in situ nanosized TiB2–TiC/Al master alloy. Adv. Eng. Mater. **24**, 2100731 (2022)
3. G.L. Rivera, R.E. Boeri, J.A. Sikora, Solidification of gray cast iron. Scr. Mater. **50**, 331–335 (2004)
4. D.M. Stefanescu, Microstructure evolution during the liquid/solid transformation in cast iron. Cast Iron Sci. Technol. (2017). https://doi.org/10.31399/ASM.HB.V01A.A0006304
5. P. Zhu, R.W. Smith, The use of thermal analysis to predict the microstructure of cast iron. in *International Symposium on Solidification Processing*, ed. by F. Weinberg (Elsevier, 1990), pp. 304–318. https://doi.org/10.1016/B978-0-08-040413-4.50032-4
6. E. Stefan, M. Chisamera, I. Riposan, S. Stan, Graphite nucleation sites in commercial grey cast irons. Mater. Today Proc. **45**, 4091–4095 (2020)
7. P. Basutkar, S. Yew, C. Loper, Effect of certain addition to the melt on the As-cast dendritic microstructure of gray cast iron. AFS Trans. **77**, 321–328 (1969)
8. G. Wang, X. Chen, Y. Li, Z. Liu, Effects of inoculation on the pearlitic gray cast iron with high thermal conductivity and tensile strength. Materials (Basel) **11**, 1876 (2018)
9. M. Gelfi, D. Gorini, A. Pola, G.M. La Vecchia, Effect of titanium on the mechanical properties and microstructure of gray cast iron for automotive applications. J. Mater. Eng. Perform. **25**, 3896–3903 (2016)

10. W. Xu, M. Ferry, Y. Wang, Influence of alloying elements on As-cast microstructure and strength of gray iron. Mater. Sci. Eng. A **390**, 326–333 (2005)
11. J.H. Park, Y. Kang, Inclusions in stainless steels—a review. Steel Res. Int. (2017). https://doi.org/10.1002/srin.201700130
12. K.O. Findley, R.L. Cryderman, A.B. Nissan, D.K. Matlock, The effects of inclusions on fatigue performance of steel alloys. Iron Steel Technol. **10**, 234–244 (2013)
13. S.N. Lekakh, Effect of nonmetallic inclusions on solidification of inoculated spheroidal graphite iron. Int. J. Metalcast. **13**, 47–57 (2019)
14. S. Chakraborty, R.J. O'Malley, L. Bartlett, M. Xu, Removal of alumina inclusions from molten steel by ceramic foam filtration. Int. J. Metalcast. (2021). https://doi.org/10.1007/s40962-020-00537-9
15. I. Riposan, M. Chisamera, S. Stan, T. Skaland, Graphite nucleant (microinclusion) characterization in Ca/Sr inoculated grey irons. Int. J. Cast Met. Res. **16**, 105–111 (2016). https://doi.org/10.1080/13640461.2003.11819567
16. I. Riposan, M. Chisamera, S. Stan, C. Hartung, D. White, Three-stage model for nucleation of graphite in grey cast iron. Mater. Sci. Technol. **26**, 1439–1447 (2010)
17. *ASTM A48 Standard for Gray Iron Castings* (ASTM International)
18. K. Balasubramanian, L.N. Bartlett, R. O'Malley, S. Chakraborty, M. Xu, Filtration efficiency of inclusions in lightweight FeMnAl steels. Int. J. Metalcast. **14**, 328–341 (2020). https://doi.org/10.1007/s40962-019-00372-7
19. M. Chisamera, I. Riposan, S. Stan, D. White, G. Grasmo, Graphite nucleation control in grey cast iron. Int. J. Cast Met. Res. **21**, 39–44 (2008)
20. E. Carter, J. Qing, M. Xu, Comparison of microstructure and non-metallic inclusions in top-filled and bottom-filled gray iron castings. AFS Trans. **132**, Paper 24–130 (2024)